JOURNAL OF MATERIALS SCIENCE **35** (2000) 723–734

A comparison of indentations of different size and geometry in single-quasicrystalline AlPdMn

B. WOLF
TU Dresden, Institut für Kristallographie und Festkörperphysik, 01062 Dresden, Germany
E-mail: wolf@physik.phy.tu-dresden.de

M. SWAIN
Commonwealth Scientific and Industrial Research Organization (CSIRO), Division of Applied Physics, National Measurement Laboratory, Lindfield, NSW 2070, Australia

M. KEMPF
Universität des Saarlandes, Institut für Werkstoffwissenschaften, 66041 Saarbrücken, Germany

P. PAUFLER
TU Dresden, Institut für Kristallographie und Festkörperphysik, 01062 Dresden, Germany

The study compares impressions into one and the same single-quasicrystalline $Al_{70}Pd_{20}Mn_{10}$ sample (surface of fivefold symmetry) that were performed by spherical and pointed indenters (Vickers- and corner-of-a-cube-geometry) and investigated using Atomic Force Microscopy (AFM). The Meyer hardness number was found to vary with indentation size in a manner similar to materials that work harden, though this behavior must have a different physical origin: for spherical indentations the hardness number slightly increases with increasing load (Meyer hardness evolution), whereas for pyramid-shaped indenters a considerable hardness increase in case of decreasing load can be stated. Spherical indentations show little piling-up only in contrast to pointed indentations where huge elevations surrounding the indent developed. Different degrees of lateral cracking can account for this observation. In case of Vickers indentations the material breaks into segments which display mutual shearing. Distinct differences can also be noticed with respect to the volume balance between the apparent piled-up volume around the impression and the volume of the displaced material. This balance proves positive for pyramidal and negative for spherical impressions.

1. Introduction

Though quasicrystals were discovered by Shechtman *et al*. fifteen years ago [1] broad practical application of quasicrystals is still missing. Among other obstacles insufficient mechanical properties, low fracture toughness and extreme brittleness [2] in particular, prove an obstacle for industrial use. However, outstanding hardness, small friction and low adhesion make quasicrystals promising candidates for tribological application [3].

Room temperature studies of quasicrystal hardness may therefore provide data of both scientific and technological interest. Most mechanical research at room temperature has been devoted to tribology of polyquasicrystalline layers or coatings containing quasicrystalline phases [4]. If mechanical properties of single-quasicrystals are addressed recent activities are focused on investigations at elevated temperatures (>900 K) where notable degrees of plasticity were found [5]. Less attention has been paid to room temperature properties of single-quasicrystals so far, which absolutely differ from properties beyond the brittle-to-ductile transition. It seems to be accepted in common that dislocations and plasticity play a negligible role in room temperature deformation. Wollgarten *et al*. [6] performed room temperature Vickers indentations into AlPdMn single-quasicrystals and investigated the surroundings of the impressions by TEM. It turned out that the indentation resulted in randomly oriented polygrained material without phase transformation. The individual grains exhibited sizes ranging from 10 to 500 nm. No evidence for dislocation involvement in the deformation process could be found. The deformation was expected to proceed via grain boundary sliding, a picture also used in this work.

For crystalline materials it is well known that the hardness depends on both indentation size and geometry [7] owing to work hardening and differences in the stress and strain distribution around the indent. It is therefore of physical interest to study indentation

size and geometry effects in quasicrystals where the deformation at room temperature differs from classical plastic deformation phenomena.

In order to obtain comparable results the use of one and the same sample in all experiments is desirable. Sample dimensions of some millimeters are required to facilitate x-ray orientation, to enable appropriate surface preparation, and to ensure a variety of indentations without mutual interaction. Thus icosahedral $Al_{70}Pd_{20}Mn_{10}$ (in the following referred to as AlPdMn for short), from which single-quasicrystalline material in large quantities (cm^3-range) is available [8], has been chosen as a test specimen.

The brittle-to-ductile transition temperature of AlPdMn is 0.87 T_m [9] (T_m: homologous melting temperature), which is comparable to other quasicrystals, but very high if compared to crystalline materials. Below T_m the hardness is much higher than the values of the elemental constituents but even higher than those of the corresponding intermetallic compounds [10]. In deformation experiments above 0.8 T_m strong work softening was observed [5]. It is therefore desirable to supplement the results presented in this paper by hardness studies in this temperature range in order to investigate the influence of work softening on indentation size and geometry effects. This has to be the subject of a separate work since the high temperatures require special precautions to avoid indenter damage.

2. Experimental conditions

The AlPdMn material under investigation was manufactured by Czochralski technique at IFF/Forschungszentrum Jülich [8]. From a single-quasicrystalline cylinder (normal parallel to the axis of fivefold symmetry) a spherical disc of 6 mm in diameter and 2 mm in thickness was cut by a diamond wire saw. The sample surface was then ground by SiC paper and polished using diamond suspension involving preparation steps of 6, 3, 1 and 0.3 μm finish. The Laue backscattering technique was used to check the sample orientation in normal and azimuthal direction.

Since nanoindentations with penetrations smaller than 20 nm were performed the quasicrystallinity close to the surface had to be checked. AES depth profiling using a PHI microprobe and Ar^+-ion sputtering revealed an oxide layer of about 3 nm thickness, mainly consisting of Al_2O_3 (Fig. 1). The oxide layer thickness was estimated from both bulk signal attenuation of the AES-peaks of Al (unoxidized) and Pd, and from the sputtering time necessary to remove the oxide.

A chemical composition according $Al_{70}Pd_{20}Mn_{10}$ is—however—no sufficient proof for the corresponding quasicrystalline phase. From x-ray diffraction under grazing incidence [11] (in order to obtain increased surface sensitivity) a phase purity of more than 90% within the analyzed subsurface layer of 200 nm thickness could be inferred resulting to the conclusion that a distorted layer—if it exists—should be thinner than 20 nm. Thus the nanohardness data presented in this paper should reflect the properties of the quasicrystalline phase.

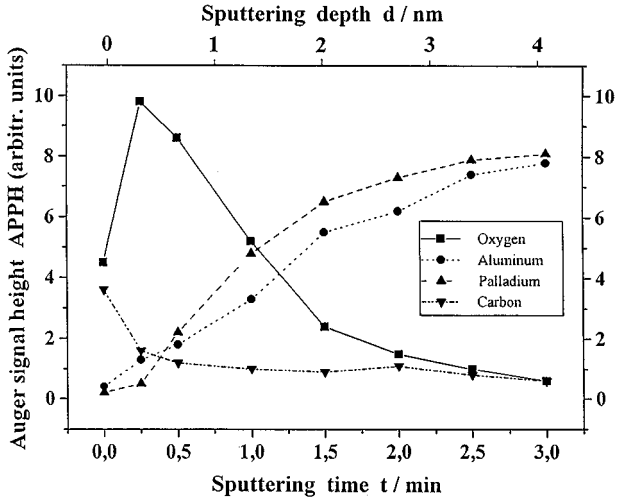

Figure 1 AES depth profiling of the AlPdMn surface after polishing: The Auger peak-to-peak heights (APPH values) of Pd, Al (unoxidized, i.e. without chemical shift), *O* and *C* are shown versus sputter time (lower scale), and versus depth (upper scale).

At TU Dresden a microhardness tester after Hanemann attached to an optical microscope (Zeiss Neophot II) was used for Vickers indentations in the force range of 0.1 to 1 N.

Nanoindentations (corner-of-a-cube diamond indenter, force range 0.1 to 7 mN) were performed using a Hysitron electrostatic transducer attached to a TopoMetrix Explorer AFM. The basic constituent of this system is a three plate capacitor the mid plate of which carries the diamond mounted onto a stylus. A voltage between the mid and the outer drive plate permits to generate a defined driving force for indentation, whereas the capacity serves as a length sensor. Further details of the Hysitron hardness tester are described in ref. [12]. The experiments with the Hysitron system took place at Institut für Werkstoffwissenschaften, Universität des Saarlandes, Saarbrücken.

For spherical indentations a UMIS 2000 submicrometer indentation system was taken advantage of at CSIRO, Division of Applied Physics, Lindfield, Australia. In this machine a spheroconical diamond indenter based on a 90° cone was applied. The radius of curvature was 5 μm as examined by SEM and temporarily *in situ* checked by indentation of standard samples. The UMIS tester was run in the multiple partial unloading mode, using an unloading of 50% after each increment in load. For further details of the indenter and extended discussion of the technique see refs. [13, 14].

In case of Vickers testing the microhardness was obtained from the impression area as determined afterwards by optical microscopy and AFM. The other techniques involved *in situ* depth sensing which permits the recording of the load-penetration-curve for both loading and unloading. The impression area (contact area) can be inferred from contact depth and indenter geometry after appropriate correction for elastic recovery, hence there is no direct need for impression imaging which requires time-consuming relocalization of the indents. On the other hand the elastic modulus is also accessible from these measurements. For comparison

the impression area was determined by AFM in those cases where the indents could be relocalized.

The time schedule of all indentations with pyramidal indenters was 15 s loading, 10 s holding of the load, and 15 s unloading. Under these conditions thermally induced phase transformations in the vicinity of the indent can be excluded unless the dimension of the impression is in the mm-range. This statement is based on the following consideration: An upper limit of the heat Q created by indentation during loading time τ is

$$Q \approx HV \approx Hh_p^3 \tag{1}$$

with H being the (average) hardness and V the volume of the displaced material. V is of the order of h_p^3 (h_p: penetration depth). The heat diffusion length L_Q may be written

$$L_Q = (\tau\lambda/\rho c)^{1/2} = (\tau a)^{1/2} \tag{2}$$

with: λ: heat conductivity, ρ: density, c: specific heat capacity, a: temperature conductance. Within the time τ the heat Q spreads into a volume V_Q according to

$$V_Q = A_0 L_Q \approx h_p^2 L_Q$$
$$(h_p \gg L_Q,\ A_0\text{: superficial impression area}) \tag{3}$$

$$V_Q = 2/3\,\pi L_Q^3 \approx L_Q^3 \quad (h_p \ll L_Q) \tag{4}$$

The mean temperature raise ΔT is then given by

$$\Delta T = Q/\rho V_Q c \tag{5}$$

$$\Delta T = (H/\rho c)(h_p/L_Q) = \gamma(h_p/L_Q); \quad (h_p \gg L_Q) \tag{6}$$

$$\Delta T = (H/\rho c)(h_p/L_Q)^3 = \gamma(h_p/L_Q)^3; \quad (h_p \ll L_Q) \tag{7}$$

The abbreviation γ has been used for $H/\rho c$. It turns out that ΔT scales with (h_p/L_Q) for $h_p \gg L_Q$, and with $(h_p/L_Q)^3$ for $h_p \ll L_Q$. For $H = 10$ GPa, $\rho = 5 \times 10^3$ kg m^{-3}, and $c = 2 \times 10^2$ J/(kg K) we obtain $\gamma = 10^4$ K. For $\tau = 15$ s and $\lambda = 1$ W/(m K) the heat diffusion length L_Q amounts to $L_Q = 4$ mm. Thus the criterion $h_p \ll L_Q$ is fulfilled in all our experiments. For penetrations smaller than 4 μm the temperature raise is less than 10^{-5} K. (A penetration of 1 mm, however, may result in melting of the impressed material.) The outcome of the above considerations is that some possible structural changes must be pressure induced rather than originating from thermal processes.

AFM investigations were performed using a commercial Nanoscope III (dimension 3000) atomic force microscope of Digital Instruments.

3. Results and discussion

3.1. Evolution of hardness number

For a better comparison of hardness data obtained from impressions of different geometry the Meyer hardness, i.e. the force over the impression projection area, is exclusively used in the following. This unit has the physical meaning of the mean pressure inside the deformation zone. Vickers and Brinell hardness are defined according force over superficial impression area. The latter is based on the indenter geometry, whereas the impression itself may considerably differ from the indenter shape, particularly in case of small indentations (shallowing, sample anisotropy). For this reason Vickers and Brinell hardness values in the original sense are difficult to handle and to compare.

3.1.1. Vickers microhardness

The Vickers mean pressure exhibits a slight tendency of hardness increase with decreasing load in the investigated force range from 0.1 to 1.2 N. The mean pressure is 9.6 and 9.1 GPa for 0.1 and 1.2 N load, respectively. The impression projection area was gained from the diagonals measured by both optical microscopy and AFM.

3.1.2. Spherical indentation

Fig. 2 displays a typical load-penetration-curve for a maximum force of 100 mN. The upper curve (crosses) represents the full-load-data, whereas the lower curve (squares) comprises the "half-load-points", since an unloading of 50% was performed after each increment in force. According Hertz the unloading curve is theoretically described by a (force F) $\sim$ (depth h)$^{3/2}$ law [15]. This relation is in practice well obeyed, even in case of deviations from spherical indenter geometry (see also next subchapter). Thus an unloading curve $F \sim h^{3/2}$ can be fitted to each pair of points (load; load/2) as represented by the bold curve for an example in Fig. 2. The partial unloading permits to determine the stiffness and the true contact area for every data point, hence allowing for the calculation of depth depending hardness and elastic modulus. With the following notion: h_{f1}: penetration depth under full load; h_{hu}: penetration depth after half unloading; h_{fu}: penetration depth after full unloading; δ: elastic recovery; F: load; R: sphere radius, we obtain:

$$\delta = h_{f1} - h_{fu} \tag{8}$$

$$F = \text{const}\,\delta^{3/2} \tag{9}$$

$$\frac{F}{2} = \text{const}\,(h_{hu} - h_{fu})^{3/2} \tag{10}$$

$$\delta = (h_{f1} - h_{hu})/(1 - 0.5^{2/3}) = 2.703(h_{f1} - h_{hu}). \tag{11}$$

Equation 11 permits the determination of the full elastic recovery for each set of measured data (F, h_{f1}, h_{fu}). According Hertz [15] the contact depth h_p may be written

$$h_p = h_{fu} + \frac{\delta}{2}; \tag{12}$$

the chordal radius r of the impression is then

$$r = (h_p(2R - h_p))^{1/2} \approx (2Rh_p)^{1/2} \tag{13}$$

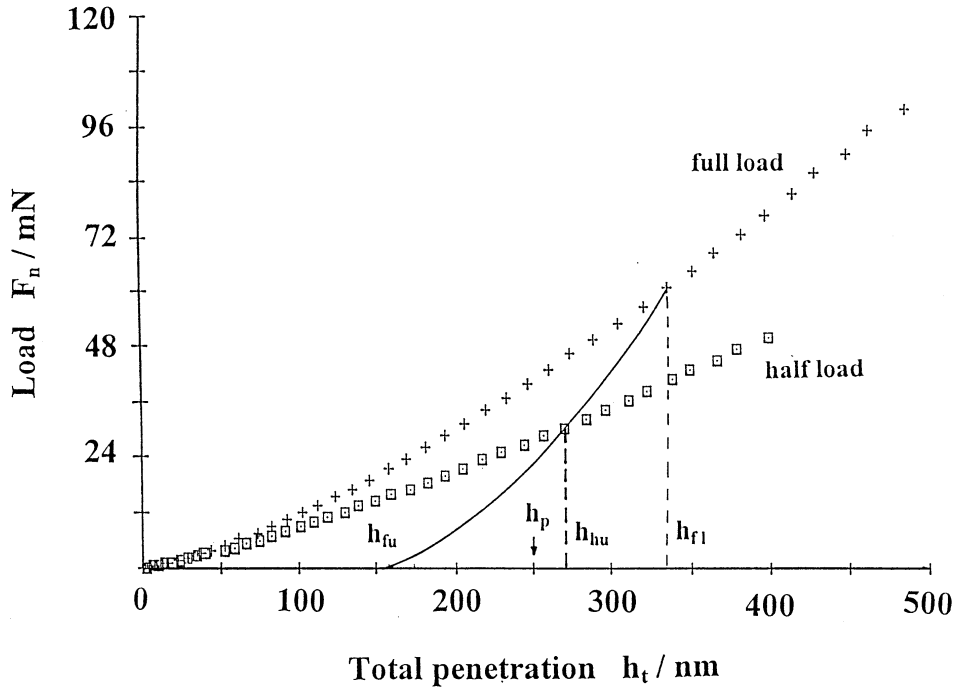

Figure 2 Force-penetration-plot for a spherical indentation test with multiply partial unloading (50% unloading after each increment in load). The crosses represent the total penetration, whereas the squares indicate the remaining penetration after 50% unloading (h_{hu}). The fit of a full unloading curve with the indication of h_{f1}, h_{hu}, h_{fu} and h_p is drawn for an example.

and the contact area A_c becomes

$$A_c = \pi h_p(2R - h_p) \approx 2\pi R h_p. \qquad (14)$$

The stiffness S_i of initial unloading is given by

$$S_i = (dF/dh)_i = (3/2)(F/\delta) \qquad (15)$$

and is related to the contact area A_c and to the effective modulus E_r according to

$$S = 2E_r(A_c/\pi)^{1/2} = 2E_r r, \qquad (16)$$

where

$$E_r = (S_i/2)/(A_c/\pi)^{1/2} = 3F/4r\delta = 3/4H(\pi A_c)^{1/2}/\delta. \qquad (17)$$

The effective modulus E_r describes the situation whereby both sample and indenter are deformed elastically. E_r is defined according to

$$1/E_r = \left(1 - \nu_i^2\right)/E_i + \left(1 - \nu_s^2\right)/E_s \qquad (18)$$

with subscript i denoting the indenter and s the sample (ν: Poisson number). The diamond related data are $\nu = 0.07$ and $E = 1140$ GPa [16]. From literature the following AlPdMn bulk data have been determined: $\nu = 0.25$ and $E = 182$ GPa [17].

The results of our calculation are shown in Fig. 3, where the modulus and the mean pressure (hardness) are plotted versus penetration depth (Fig. 3a and b, respectively). The constant value of E close to the literature value [17] indicates, that the experimental results are reliable. Furthermore the material is homogeneous with depth, and the E-determination is not affected by cracking. The slight deviation close

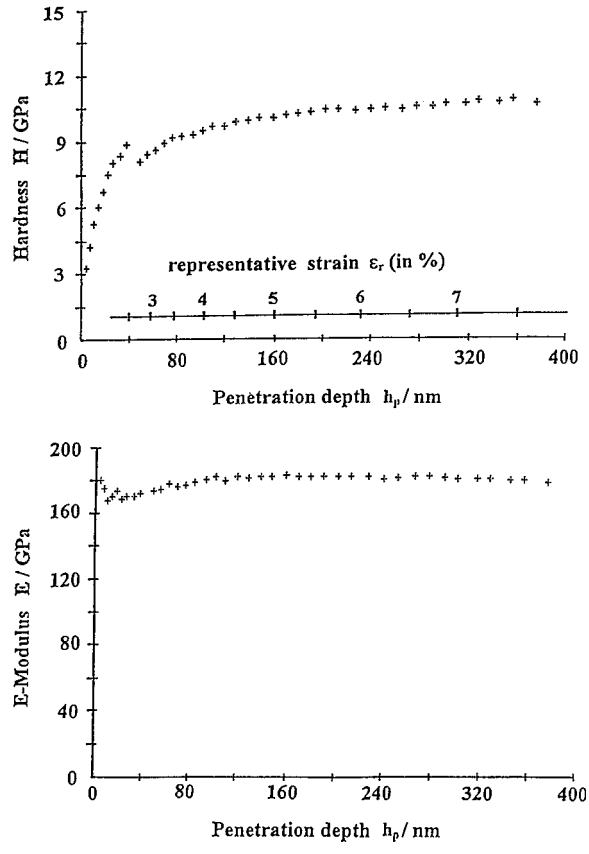

Figure 3 Depth dependent hardness (mean pressure, upper part) and corresponding values of the E-modulus (lower part) as derived from data of Fig. 2.

to the surface may be attributed to the oxide surface layer. A discontinuity in H occurs when exceeding a penetration depth of about 30 nm. The origin of this repeatable effect may be the onset of irreversible ("plastic") deformation (see also below).

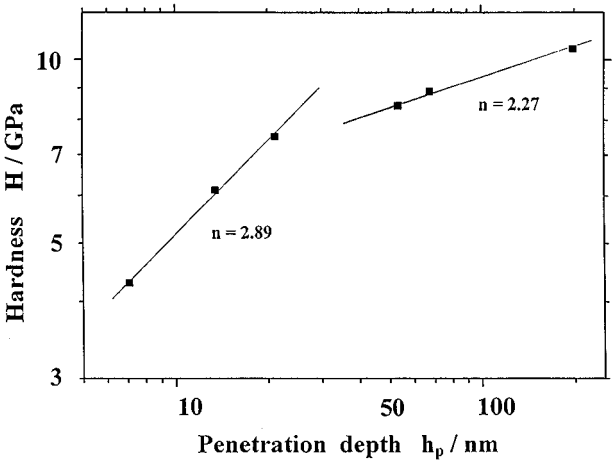

Figure 4 Log-log-plot of hardness versus penetration for Meyer analysis (spherical indentation).

The hardness increases with increasing load. This behavior is typical for materials that work harden since deeper penetration results in higher amounts of plastic strain. For these materials Meyer [18] found a relation between load and contact area:

$$F \sim d^n/D^n; \quad H \sim d^{n-2} \tag{19}$$

with denotions: d: chordal diameter of the impression; D: indenter diameter. Introducing the relation $d^2 = 4h_p(2R - h_p) \approx 8Rh_p$ in accordance with Equation 6 we obtain

$$H \sim h_p^{(n/2)-1}; \quad F \sim h_p^{n/2} \tag{20}$$

The number n is the so called Meyer index, that varies for "ordinary" metals between 2 (constant hardness, i.e. fully work hardened material) and 2.6 (strong work hardening, i.e. annealed material). In case of work softening $n < 2$ should be observed. For pure elastic contacts and shallow spherical impressions $F \sim h_p^{3/2}$ is obtained, and h_p can be expressed according to $h_p = d^2/8R$, resulting in $F \sim d^3$. From Equation 12 it can be deduced that n amounts to 3 in this case. The Meyer index n can be obtained from a log-log-plot of force or hardness versus contact depth.

The application of Meyer analysis to our measurement is depicted in Fig. 4. For penetration depths below 30 nm a Meyer index $n_1 = 2.89$ is found, for deeper penetrations n changes to $n_2 = 2.27$. The application of Meyer analysis to quasicrystal deformation is very formal, since plasticity in its common sense is not involved in the deformation process. Nevertheless one can differentiate between regions of qualitative and quantitative differences. Since n_1 is very close to 3 it seems reasonable to assume that for penetrations smaller than 30 nm the deformation is purely elastic. This prediction shall be considered in the light of the force threshold F_{thr} necessary to initiate first plastic deformation. According to [13, 19] F_{thr} writes

$$F_{thr} = (9/16)(3\pi Y)^3(R/E_r)^2, \tag{21}$$

and the corresponding threshold in depth $h_{p,thr}$ is equivalent to

$$h_{p,thr} = (9/32)(3\pi)^2(Y/E_r)^2 R \approx 25(Y/E_r)^2 R. \tag{22}$$

Unfortunately, the yield stress Y at room temperature is not known. When applying the relation between Y and the macroscopic hardness H,

$$H \approx 3Y, \tag{23}$$

Y would amount to about 3 GPa. This in combination with $R = 5$ μm and $E_r \approx 200$ GPa results in $F_{thr} = 7.9$ mN and $h_{p,thr} = 28$ nm in surprisingly good agreement to the coordinates of the discontinuity in H.

3.1.3. Corner-of-a-cube nanoindentations

For this type of experiments a pyramidal diamond indenter with triangular cross section was used. Its geometry is that of a corner of a cube; we will speak of CC-Berkovich for short (the denotation "Berkovich" shall indicate that its cross section is a equilateral triangle as applies to the classical "Berkovich" too). This indenter is much sharper than the classical Berkovich one which is best expressed by the area function $A(h)$, i.e. the cross section area A as a function of distance h from the tip for the ideal geometry. For pyramidal indenters with an equilateral triangle being the cross section $A(h)$ is given by

$$\begin{aligned} A(h) &= 3 \times (3)^{1/2} h^2 \tan^2 \alpha \\ &= \left(\frac{3}{4}\right) \times (3)^{1/2} h^2 \tan^2 \beta \end{aligned} \tag{24}$$

with: α: angle between the axis of the pyramid and the axis of a side plane (apical face angle) and β: angle between the axis of the pyramid and an edge.

Vickers and Berkovich tester have the same idealized area function

$$A(h) = 24.51h^2 \tag{25}$$

whereas a relation

$$A(h) = 1.5 \times (3)^{1/2} h^2 = 2.598h^2 \approx 2.6h^2 \tag{26}$$

applies to the CC-Berkovich indenter ($\alpha = 35.3^\circ$, $\beta = 54.7^\circ$, $\alpha + \beta = 90^\circ$). Thus for equivalent load and hardness the penetration depth of a Vickers or Berkovich tester is $(2.598/24.51)^{1/2} = 32.6\%$ of the CC-Berkovich indenter only. The advantage of the sharp CC-Berkovich geometry is, that it can be used for both indentation and imaging of the resulting impression. One must, however, admit that imaging of the impression with the tool of impression generation is not suitable for precise area measurement. Nevertheless coarse imaging using the indenter permits to position the indents; and it is also useful for relocalization of the impressions when scanning the impression field later on using finer tips. The main disadvantages of the CC-geometry are

- the hardness values differ from measurements with conventional geometry,
- relatively little literature data exists for comparison, and
- crack formation and piling up are enhanced, i.e. assessed E-moduli are less reliable.

The Meyer hardness (mean pressure) H_M can in general be written like

$$H_M = CY \tag{27}$$

with Y denoting the plastic yield stress in simple tension or compression, and C being a dimensionless constant depending on the indenter geometry. In early experiments of Tabor *et al*. [7] an increase of C with decreasing apex angle of a cone was established as depicted in Fig. 5. This also explains the hardness raise for increasing penetration in Brinell tests since the "effective" apex angle of the inserted part of the sphere gets reduced. Thus the hardness values obtained in CC-Berkovich test can be expected to be larger than those obtained in tests of more blunt geometry. In Table I some representative results of the CC-Berkovich test are summarized. The calculation is based on an indenter modeling according Fig. 6, i.e. a cap of a cone was fitted to the trunk of the pyramid. The algorithm for H_M and E_r calculation is the following:

From the loading-unloading-curve the depth of the remaining plastic deformation h_r after full unloading, the total penetration depth for full load h_t, and the elastic recovery $\delta = h_t - h_r$ are taken. The unloading curve is fitted by a power $F \sim h^n$ (h: elastic penetration). Following the suggestion of Oliver and Pharr [20] the total elastic recovery is then separated into two parts: δ_o outside the impression and δ_i inside the impression:

$$\delta_o = \delta\varepsilon/n, \quad \delta_i = \delta(1 - \varepsilon/n). \tag{28}$$

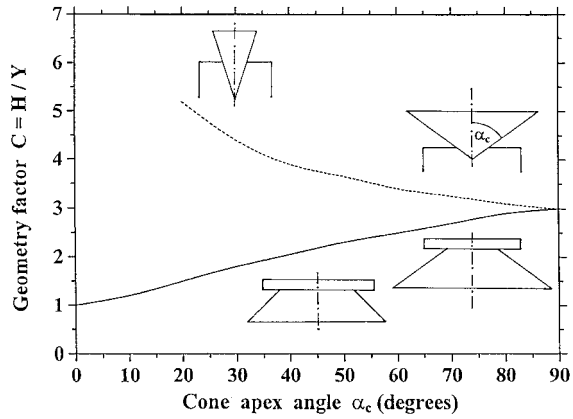

Figure 5 Hardness (mean pressure) dependence on deformation geometry: The hardness expressed in units of yield strength Y (thus representing the factor C of Equation 17) is drawn versus cone apex angle for penetration of a conical indenter into a flat sample (upper curve), and for deformation of a conical sample by a planar "indenter" (lower curve). Experimental values for copper deformed by steel, taken from Tabor (ref. 7). The inserted pictures shall illustrate the experimental situations.

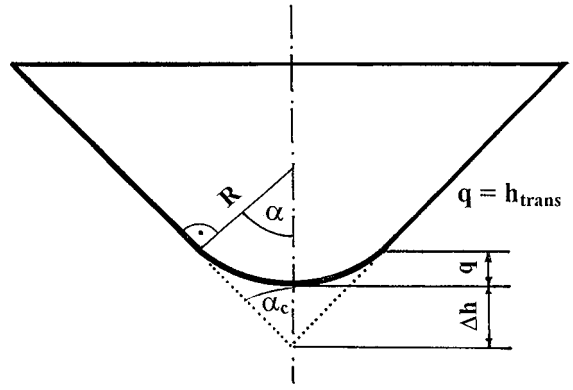

Figure 6 CC-Berkovich indenter geometry modeling as used in this work: the pyramidal indenter was replaced by a cone of equivalent idealized area function $A(h)$ and fitting a cap of a sphere to its end.

TABLE I Hardness and E-modulus results for a CC-Berkovich test in AlPdMn

F (mN)	h_r (nm)	δ (nm)	h_p (nm)	h_p^* (nm)	A_c^c (μm^2)	H^c (GPa)	E_r^c (GPa)	A_c^{sp} (μm^2)	H^{sp} (GPa)	E_r^{sp} (GPa)
Blunting radius $R = 50$ nm										
6	284	72	320	344	0.308	19.5	200	*0.100*	*60.0*	*349*
4	220	55	248	272	0.192	20.8	220	*0.078*	*51.3*	*346*
2	133	40	153	177	0.081	24.7	234	*0.048*	*41.6*	*303*
1	57	26	70	94	0.023	43.5	338	*0.022*	*45.5*	*345*
0.5	23	18	32	*56*	*0.008*	*61.3*	*306*	0.010	49.7	367
Blunting radius $R = 130$ nm										
6	284	72	320	384	0.383	15.7	179	*0.253*	*23.7*	*220*
4	220	55	248	312	0.253	15.8	192	*0.202*	*19.7*	*214*
2	133	40	153	217	0.122	16.3	189	0.125	16.0	188
1	57	26	70	*134*	*0.0467*	*21.4*	*237*	0.0571	17.5	214
0.5	23	18	32	*96*	*0.0240*	*20.9*	*239*	0.0253	19.8	232

Most probable hardness values					
F (mN)	6	4	2	1	0.5
H (GPa)	16	16	16	18	20

F: load; h_r: remaining plastic depth after complete unloading; δ: elastic recovery; h_p: contact depth; h_p^*: contact depth extended by Δh (blunting correction), A_c: contact area; H: hardness; E_r: effective E-modulus. The superscript c refers to the model of the pure cone, and the superscript sp corresponds to the model of the pure sphere. The data in italics are not relevant since the considered depth region is either below h_{trans} for the model of the pure cone, or above h_{trans} for the model of the pure sphere. For a blunting radius of $R = 50$ nm the calculated moduli are always too high, and no continous transition between the datasets (A_c^c, H^c, E_r^c) and (A_c^{sp}, H^{sp}, H^{sp}) is possible. For a blunting radius $R = 130$ nm the E-moduli are in the range of the literature data, and for a load of $F = 2$ mN the considered datasets are almost equivalent.

The dimensionless number ε is a geometry factor which should be 0.72 for a conical or pyramidal indenter and 0.75 for a spherical or parabolic indenter geometry. One must however admit that the geometry influence on elastic recovery is not simply governed by the indenter alone, but determined by the geometry of the system (indenter + plastically or in another way inelastically deformed zone). Since the plastic deformation zone is more or less spherical in most cases the elastic recovery after conical or pyramidal indentation resembles more that of a ball indentation. This is also reflected by the power index n, which is often close to 1.5 instead of 2, as it should be for pointed indentation [21]. In our experiments n varied between 1.42 and 1.48, confirming, that the consideration above also applies to quasicrystals. For ε a value of $\varepsilon = 0.735$ as a compromise between the two extremes was used in this work. The contact depth or effective plastic depth h_p is then obtained according to

$$h_\mathrm{p} = h_\mathrm{r} + \delta_\mathrm{i} = h_\mathrm{t} - \delta_\mathrm{o}. \tag{29}$$

For the small penetrations, regarded in this work, tip truncation must be quantitatively taken into account. We modeled the blunted pyramidal indenter by a trunk of a cone (apex angle α_c) in such a way that pyramid and cone have the same idealized area function $A(h_\mathrm{p}) = 2.6h_\mathrm{p}^2$. Since the area function of the cone writes

$$A(h_\mathrm{p}) = \pi h_\mathrm{p}^2 \tan^2 \alpha_\mathrm{c} = 2.6h_\mathrm{p}^2 \tag{30}$$

the corresponding apex angle amounts to $\alpha_\mathrm{c} = 42.3^\circ$. The cone has the advantage that a cap of a sphere can be fitted to its trunk without shape discontinuities. Since the transition from the real indenter pyramid to its spherical end can be expected to be comparatively smooth the suggested modeling seems to be a reasonable approach. The transition from sphere to cone takes place in a height h_trans (Fig. 6). Hence we have

$$h_\mathrm{trans} = q = R(1 - \cos\alpha) = 0.3218R \tag{31}$$

$$\alpha = 90^\circ - \alpha_\mathrm{c}. \tag{32}$$

A coarse value of h_trans can also be assessed from a discontinuity of the first derivative of the loading curve, the low-load-part of which is nearly linear (the loading curve of a sphere into a fully plastic body of constant hardness is a straight line), whereas the high-load-part is more parabolic (the loading curve of a pyramid/cone into a fully plastic body of constant hardness is a parabola). The hardness calculation requires therefore to decide between two situations: For $h_\mathrm{p} < h_\mathrm{trans}$ the model of the pure sphere is used; the contact area writes now

$$A_\mathrm{c} = \pi\left(2Rh_\mathrm{p} - h_\mathrm{p}^2\right) \approx 2\pi Rh_\mathrm{p}. \tag{33}$$

For $h_\mathrm{p} > h_\mathrm{trans}$ the area function of the ideal geometry of the corner of the cube can be used when adding a height supplement Δh to the contact depth to correct the data for tip blunting (Fig. 6, the superscript * shall indicate that the value is converted to the model geometry):

$$\Delta h = R((\cos\alpha)^{-1} - 1) = 0.4745R \tag{34}$$

$$h_\mathrm{p}^* = h_\mathrm{p} + \Delta h, \quad A_\mathrm{c} = 2.6h_\mathrm{p}^{*2}. \tag{35}$$

A critical point proves to be the correct blunting radius R, which was determined in an iteration procedure. A starting value of R was estimated from the smallest details in the AFM images when scanning with the indenter. Then R was varied around this value to best fulfill the following criteria:

- hardness and E-modulus data for the transition height h_trans inferred from the trunk-of-a-pyramid model should be equivalent to those using the pure sphere model.
- h_trans should agree to the transition between the more linear and the more curved part of the loading curve.
- the values of E_r should be correct. Particularly for very small penetration depths, when larger cracking is avoided, the measured E_r should converge against the value determined as a bulk property by nondestructive techniques (the rectangular parallelepiped resonance method, e.g.).

The mentioned criteria were best fulfilled for $R = 130$ nm. Literature data of E for AlPdMn are in the range of $E = 180$–200 GPa ($E = 182$ GPa [17]; 190 GPa [8]; 200 GPa [22]), resulting in $E_\mathrm{r} = 190$–210 GPa. The apparent reduction of E_r for higher forces may be attributed to the crack formation. The hardness exhibits a distinct increase with decreasing load. The absolute hardness value for 7 mN, the highest load the electrostatic transducer can generate, is about 16 GPa, about 70% higher than the Vickers microhardness and about 50% higher than the Brinell ultramicrohardness for 100 mN. Without filling the force gap between 10 mN and 1 N by Vickers and CC-Berkovich tests one cannot say to what extend the difference is an indentation size effect or an indenter shape effect, respectively. The further increase of hardness to values of about 20 GPa when reducing the load leads to the assumption that both effects are likely to contribute to the hardness number evolution.

The hardness increase for smaller forces may be interpreted in terms of the Hall-Petch relation [23] which was found with nanostructured materials:

$$H = \sigma_0 + k_0 L^{-1/2} \tag{36}$$

where σ_0 is the intrinsic stress, resisting dislocation motion, k_0 a constant, and L a characteristic grain dimension. Thus the hardness increases with smaller grains. If the deformation in quasicrystals is based on grain boundary sliding, and if larger impression forces result in formation of larger grains, then a mechanism similar to that in nanostructured materials can lead to increased ductility for higher forces.

A further source of hardness increase with decreasing load may be the reduced number of induced cracking.

This was demonstrated in a recent paper of Swain *et al*. who investigated the hardness of amorphous glassy carbon by Vickers and CC-Berkovich tests [24]. The hardness could be shown to increase with decreasing apical face angle of the indenter, which has two reasons: the different stress fields in case of varying apex angles, and the fact, that the sample gets more susceptible for radial crack initiation with sharper indenters. For the corner-of-a-cube indenter a strong indentation size effect was found: the hardness increases by about 50% when reducing the load from 1 N to about 20 mN, which is similar to our findings.

3.2. Morphology of the impression environment

Inspecting the resultant impressions by AFM reveals drastic differences between indentations with a penetration depth small compared to the radius of curvature R of the hardness tester (type-I impressions: spherical indentations, scratching with a spheroconical needle) and those, where the plastic depth is much larger than R (type-II impressions: pyramidal indentations). The task of this section is to describe the differences and to make an attempt of explanation.

The material displaced by the indenter cannot disappear. In some rare cases transitions to phases of higher density occur [25], in all other cases the displaced volume must be somehow "accommodated". To some extent displaced material can be elastically accommodated by trapped stresses [26], most of the displaced matter is in general relocated in the piling-up structures. Crystalline materials often exhibit long range surface modifications around the indent where the displaced material is gently smeared out over large areas.

Our AFM inspection of type-II impressions shows that surface modifications are restricted to the close vicinity of the indent, where considerable amounts of material are piled up. This is easy to recognize since the quasicrystalline structure with its missing translation symmetry does not favor material displacements over large distances. On the other hand some degree of ductility seems to be involved in type-I impression, since piling up is very weak, and the outer appearance of the impressions is similar to that of ductile crystalline material.

3.2.1. Impressions of pointed indenters

When performing Vickers tests the material around the indent breaks into segments which are shifted in height by mutual shearing. This shearing occurs along radial cracks which preferentially propagate in definite quasicrystallographic directions. Fig. 7 displays an AFM height image for a symmetric positioning of the indenter with respect to the sample of fivefold symmetry, and a qualitative attempt to explain the created structures. The image exhibits a mirror plane as can be expected from the symmetry superposition. The larger or smaller divergence between sample and indenter directions gives rise to more or less constructive stress superposition resulting in high or less high segment uplifting. The morphology of Vickers impression has been the subject of our papers [27] and [28]. The outer appearance of the indentation induced elevations around the indent is very stable when repeating the tests but proves extremely sensitive to sample rotation around the specimen normal [27]. If the impression asymmetry were due to an inclined indenter, the asymmetric structures should remain fixed with respect to the indenter (i.e. fixed with respect to the image frame), if it were due to the sample crystallography alone, it should rotate together with the sample. We found, however, that the impression asymmetry rotates with four times the speed of the sample, and into opposite direction. This was explained as an angular Moiré effect resulting

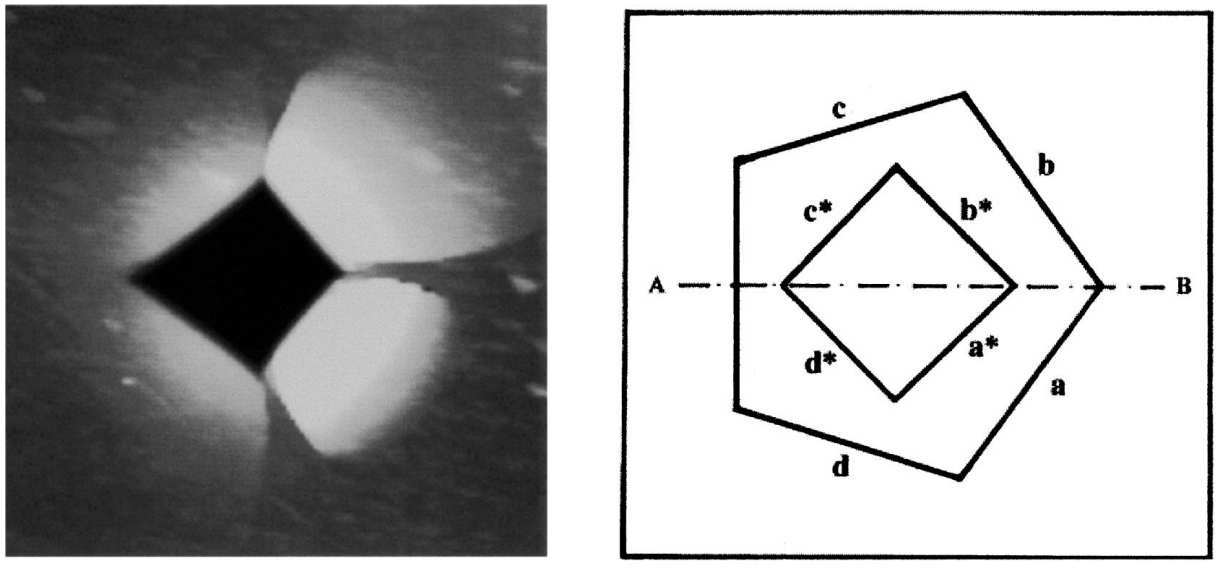

Figure 7 AFM height image of a Vickers impression (left), and schematic representation of the relative position between indenter and sample (right). The pentagon represents the position of equivalent quasicrystallographic lattice planes exhibiting two fold symmetry. The height distribution of the piled up elevations can be explained by symmetry superposition of the fourfold indenter symmetry and the fivefold sample symmetry as schematically depicted in the right drawing. The asymmetry is not due to indenter inclination as can be shown by indentations after sample rotation [27]. The dash-dot-line indicates a mirror plane which is visible in the AFM height image, too.

from the symmetry superposition of sample and indenter [27, 28].

One has to ask by what mechanism the material displacement proceeds if no dislocations are involved. In accordance with the findings of Wollgarten *et al*. [6] we assume a fragmentation into polygrained material followed by subsequent grain boundary sliding. Though no deformation mechanism on an atomic scale has hitherto become known the proposed process can be expected to be easier initiated than slip of dislocations in the bulk.

The differences between type-I and type-II impressions are based on different degrees of cracking, the formation of lateral vent cracks in particular. In type-I impressions material flow is mainly directed into the downward direction, giving rise to formation of extended regions of large hydrostatic constraint, where crack nucleation is inhibited. In type-II indentations considerable displacement towards the sides occur, particularly for indenters with small apex angles. The accomodation of this material results in residual stresses which facilitate lateral cracking upon unloading [29, 30]. The increased amount of cracking may result in fragmentation into individual grains separated by macroscopic defects as schematically depicted in Fig. 8. The stability of the indentation induced structures under constant conditions, the preferential propagation of cracks along crystallographic planes and the sensitivity to azimuth orientation changes demonstrates, however, that the fragmentation cannot be a stochastic process but must follow well defined rules.

3.2.2. Spherical indentations

Figs 9a and b display AFM height images of spherical impressions with loads of 0.5 and 0.1 N, respectively. For the high load the degree of piling up and the formation of cracks are comparable to the results obtained in case of Vickers indents. For the small load practically no piling up can be noticed. A closer look reveals small elevations that exhibit traces of fivefold symmetry. Nevertheless the relative degree of piling up is negligible if

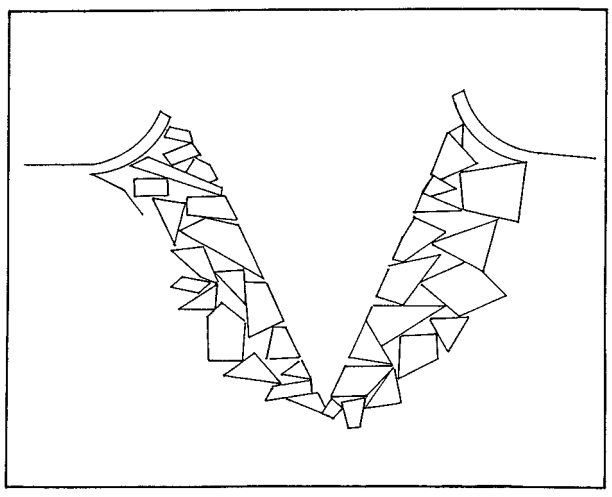

Figure 8 Schematic drawing of the indentation induced fragmentation in the vicinity of a Vickers indent. Note the bending of the topmost layer which is not subject to further disintegration.

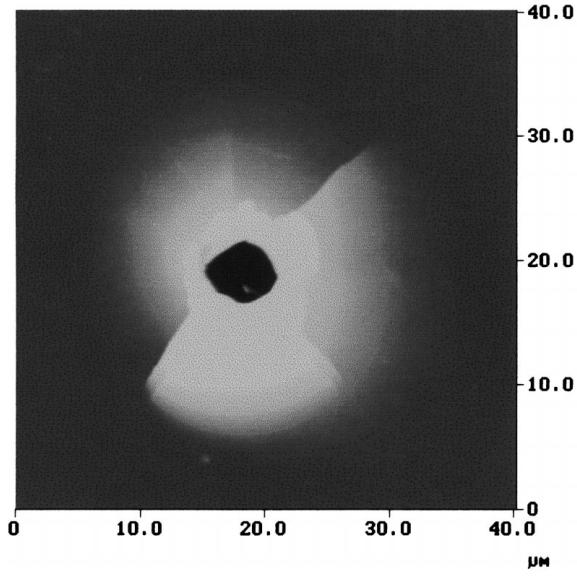

(a)

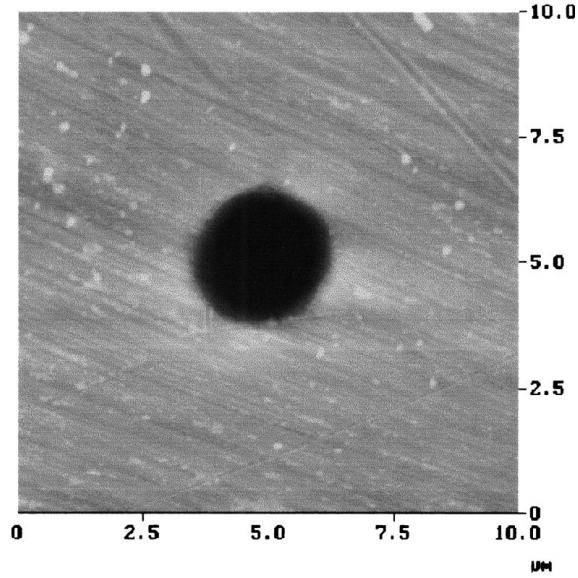

(b)

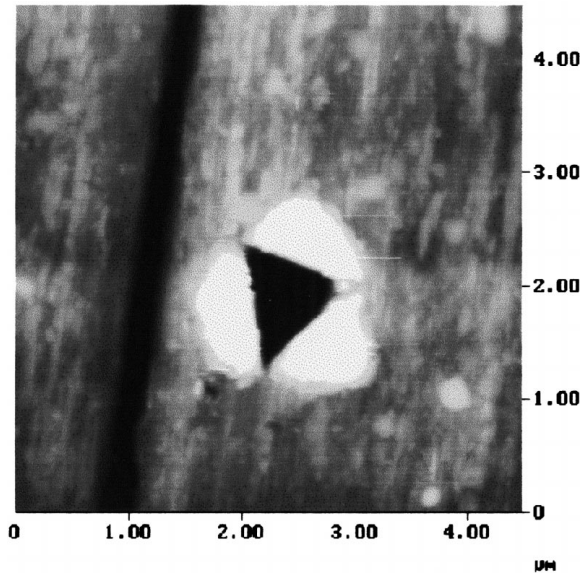

(c)

Figure 9 Comparison of piling-up formation in case of a "heavy" spherical indentation (0.5 N, 10a), a small spherical indentation (0.1 N, 10b) and a CC-Berkovich indent (5 mN, 10c). The AFM height scales are 500 nm (10a) and 80 nm (10b and c), respectively.

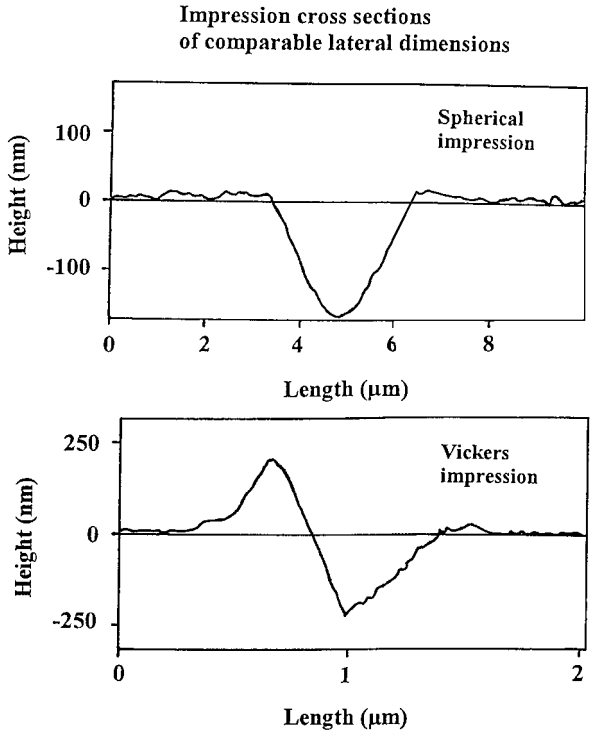

Figure 10 Comparison of cross sections through a spherical impression (top) and a CC-Berkovich impression (bottom) displaying distinguished differences in the relative height of piledup elevations from which also large differences in the volume balance between displaced and reappeared material can be assessed.

compared to the extent obtained for high load, or in case of pointed impressions. In a first thought this does not seem surprising since for "normal" materials the relative degree of piling up always decreases for smaller loads. But in our case the degree of piling up seems not to be related to the load directly, but to the effective apex angle of the impressed part of the indenter. Piled-up hillocks with heights comparable to the depth of the impression were always observed with CC-Berkovich indentations independent on load as long as the penetration depth was larger then the blunting radius.

For conventional materials a rule of thumb predicts similar degrees of piling up for similar displaced volumes. From Fig. 10, where cross sections through a spherical and a CC-Berkovich impression are displayed, one can easily conclude that this rule is not obeyed by quasicrystals in the considered force range: the piling up for the pointed impression is considerably larger though the displaced volume is even smaller than in case of the spherical one. The abundance of piling up seems to be determined by the threshold of lateral cracking depending on the nature of the sample (brittleness), the load, and the "effective" apex angle of the indenter. For the spherical impression a certain ratio (chordal diameter/indenter diameter) must be exceeded to create significant piling up, i.e. the load must be raised above a certain value for a given sphere diameter.

4. Volume balance and porosity

The availability of precise height information in AFM permits a comparison of the volume displaced by the indenter with the volume which reappears above the undisturbed surface. This comparison is—however—relative, since the measurement zero level can only be defined with respect to the surface position at the moment of measurement and not in a more generalized way. Consequently a surface uplifting over a large area by a small constant amount is not detectable.

In case of Vickers indentations the apparent volume of the piled up elevations is about 30 to 40% larger than the volume of the impression. This excess ε is due to lateral cracking and the formation of subsurface defects, which could be demonstrated by secondary indentation [27]. Furthermore a decreased contact stiffness of the elevations was detected by force modulation technique [27], which also gives evidence for hole formation in the vicinity of the indent and supports the suggested mechanism of material displacement. For the CC-Berkovich impressions the mentioned volume excess ε of elevations is even larger: an average value is $\varepsilon = 140\%$.

The level of porosity in the vicinity of the indent can be assessed using the following zero-order approach: It is assumed that the defects are concentrated within a half-sphere the diameter d_{aff} of which is equivalent to the diameter of the impression-modified surface area as recognized by AFM. The volume of this half-sphere is

$$V_{\text{aff}} = (\pi/12) d_{\text{aff}}^3. \tag{37}$$

The volume of displaced material in case of the square-shaped Vickers impression (side length a) reads

$$V_{\text{imp,V}} = a^3 \tan 22^\circ / 6 \tag{38}$$

and that in case of the CC-Berkovich (side length s of the impression triangle) is

$$V_{\text{imp,CC}} = s^3/(12(2)^{1/2}). \tag{39}$$

The volume ratio between impression affected and displaced material is then

$$V_{\text{aff}}/V_{\text{imp,V}} = (\pi/2 \tan 22^\circ)(d_{\text{aff}}/a)^3 = 3.89(d_{\text{aff}}/a)^3 \tag{40}$$

$$V_{\text{aff}}/V_{\text{imp,CC}} = \pi(2)^{1/2}(d_{\text{aff}}/s)^3 = 4.44(d_{\text{aff}}/s)^3. \tag{41}$$

The porosity P can be determined according to

$$P = (V_{\text{elevation}} - V_{\text{displaced}})/V_{\text{affected}} \tag{42}$$

$$P = (V_{\text{elevation}}/V_{\text{displaced}} - 1)/(V_{\text{affected}}/V_{\text{impression}}) \tag{43}$$

$$P = \varepsilon/(V_{\text{aff}}/V_{\text{imp}}) \tag{44}$$

with ε being the relative volume excess. For Vickers impressions we obtain $d_{\text{aff}}/a = 2.5$ as an average value, resulting in $P = 0.58\%$ ($\varepsilon = 35\%$), and for the CC-indentation d_{aff}/s amounts to 1.88, yielding $P = 4.8\%$ ($\varepsilon = 140\%$).

Contrary to the impressions of pointed indenters the volume balance for spherical indentation proved negative, i.e. about 70% of the displaced material is "missing". We can therefore conclude that for increasing

indenter apex angle the material displacement becomes more and more restricted to the close vicinity of the impression, where enlarged degrees of lateral cracking and subsurface defect formation result in large porous elevations, whereas the displaced material is smoothly distributed over larger volumes in case of shallow spherical indentations, thus not simply detectable by AFM.

5. Conclusions

The dependence of hardness on experimental conditions as load (indentation size effect, ISE), temperature (temperature softening) and loading time (creep behavior) may provide information on nanoscopic processes of inelastic deformation. We have shown elsewhere [31] that quasicrystals exhibit a negative indentation size effect at elevated temperatures, i.e. the hardness raises with increasing load. This uncommon behavior is a unique property of quasicrystals and may be attributed to quasilattice failure generation during motion of phason-type dislocations. At room temperature, however, quasicrystals behave like ordinary matter: their hardness increases with decreasing load when testing with a sharp pointed indenter. This observation is generally explained in terms of work hardening when crystalline matter is addressed. In case of quasicrystals we attribute this property to different fragmentation sizes caused by impressions of different load: high load—large fragments, small loads—tiny fragments. The hardness evolution with load may then be explained by a generalized Hall-Petch-relation according which the hardness of polygrained material increases according $d^{-1/2}$ (d: grain diameter).

For spherical indentations an increase of hardness (in the sense of indentation mean pressure) was observed when raising the load. This seems to contradict the statements above for a first thought. Actually this observation fits into the picture of the established deformation model when having following facts in mind:

- The hardness values reported here are derived from depth sensing, not from imaging. They represent the mean pressure inside the deformation zone. For high loads—when the inelastic deformation zone has fully developed—a coincidence with classical hardness—derived from mapping of the impression—may be expected. For very small loads the pure elastic properties are reflected! For indentations with the sharp pointed indenter the threshold of inelastic deformation is exceeded for all loads reported in this paper.
- When considering pyramidal indentations the impression induced fragment size is expected to scale with a characteristic length of the impression groove. This is, because the impression grooves are geometrically similar. For a spherical impression the radius of curvature of the remaining surface deformation can be used as corresponding length of comparison. And this radius of curvature decreases with increasing load: small load → strong elastic recovery → shallow deformation → small number of cracks → large fragment size → small hardness. The indentation size effect is thus described in a more coherent manner when related to a characteristic impression length rather than to the load.

Acknowledgements

Prof. K. Urban and coworkers, Forschungszentrum Jülich, are heartily thanked for providing high quality AlPdMn singlequasicrystalline material. The authors are indebted to Dr. S. Baunack, IFW Dresden e. V., for performing Auger depth profiling, and to Dr. Rhena Krawietz, TU Dresden, for x-ray characterization. Prof. H. Vehoff, Prof. U. Hartmann, Dr. R. Houbertz, Dr. M. Göken, and co-workers, Universität des Saarlandes, are acknowledged for scientific support, technical assistance and fruitful discussions concerning Atomic Force Microscopy and nanoindentations with the corner-of-a-cube indenter. One author (B. W.) would like to express his thanks to the German Academy of Natural Scientists Leopoldina Halle (Saale) which supported his work by a promotion grant and financiation of equipment purchase. Financial support by the "Deutsche Forschungsgemeinschaft" and the "Fonds der Chemischen Industrie" is also gratefully acknowledged.

References

1. D. SHECHTMAN, I. BLECH, D. GRATIAS and J. W. CAHN, *Phys. Rev. Lett.* **53** (1984) 1951.
2. M. WOLLGARTEN and K. URBAN, in "Lectures on Quasicrystals," edited by F. Hippert and D. Gratias, (Les Editions des Physiques, Les Ulis, 1994) chap. 12 p. 535.
3. S. S. KANG, J. M. DUBOIS and J. VON STEBUT, *J. Mater. Res.* **8** (1993) 2471.
4. J. VON STEBUT, C. STROBEL and J. M. DUBOIS in "Proceedings 5th Int. Conf. on Quasicrystals, Avignon, 1995," edited by C. Janot and R. Mosseri (World Scientific, Singapore, 1995) p. 704.
5. M. FEUERBACHER, R. ROSENFELD, B. BAUFELD, M. BARTSCH, U. MESSERSCHMIDT, M. WOLLGARTEN and K. URBAN, in "Proceedings 5th Int. Conf. on Quasicrystals, Avignon, 1995," edited by C. Janot and R. Mosseri (World Scientific, Singapore, 1995) p. 714.
6. M. WOLLGARTEN and H. SAKA, in "New Horizons in Quasicrystals: Research and Applications" (World Scientific, Singapore, 1997) p. 320.
7. D. TABOR, *Phil. Mag. A***74** (1996) 1207; D. TABOR, "The Hardness of Solids" (Oxford University Press, Oxford, UK, 1951).
8. M. FEUERBACHER, PhD thesis, Forschungszentrum Jülich, Rheinisch-Westfälische Technische Hochschule, Aachen, 1996.
9. J. E. SHIELD, M. J. KRAMER and R. W. MCCALLUM, *J. Mater. Res.* **9** (1994) 343.
10. L. BRESSON, in "Lectures on Quasicrystals", edited by F. Hippert and D. Gratias (Les Editions des Physiques, Les Ulis, chap. 13, 1994) p. 549.
11. RH. KRAWIETZ, personal communication, 1997.
12. B. BHUSHAN, A. V. KULKARNI, W. BONIN and J. T. WYROBEK, *Phil. Mag. A***74** (1996) 1117.
13. J. S. FIELD and M. V. SWAIN, *J. Mater. Res.* **8** (1993) 297.
14. *Idem., ibid.* **10** (1995) 101.
15. H. HERTZ, *J. reine u. angew. Mathematik* **92** (1882) 156.
16. J. E. FIELD (eds.), "The Properties of Diamond" (Academic Press, London, 1979).
17. K. TANAKA, Y. MITARAI and M. KOIWA, *Phil. Mag. A* **73** (1996) 1715.
18. E. MEYER, *Z. Verein. Deutscher Ing.* **52** (1908) 645.
19. U. DÜRIG and A. STALDER, in "Micro-/Nanotribology and its Applications," edited by B. Bhushan (Kluwer Academic Publishers, Dordrecht, 1997) NATO Series E, Vol. 330, pp. 61–99.
20. W. C. OLIVER and G. M. PHARR, *J. Mater. Res.* **7** (1992) 1564.
21. TH. CHUDOBA, PhD thesis, Forschungszentrum Rossendorf, TU Dresden, 1996.

22. Y. YOKOYAMA, A. INOUE and T. MASUMOTO, *Mater. Trans. JIM* **34** (1993) 135.
23. R. W. SIEGEL and G. E. FOUGERE, *Nano Structured Materials* **6** (1995) 205.
24. M. V. SWAIN and J. S. FIELD, *Phil. Mag. A* **74** (1996) 1085.
25. G. M. PHARR, W. C. OLIVER and D. S. HARDING, *J. Mater. Res.* **6** (1991) 1129.
26. A. PAJARES, F. GUIBERTEAU, R. W. STEINBRECH and A. DOMINGUEZ-RODRIGUEZ, *Acta metall. Mater.* **43** (1995) 3649.
27. B. WOLF, C. DEUS and P. PAUFLER, *Surface and Interface Analysis* **25** (1997) 561.
28. C. DEUS, B. WOLF and P. PAUFLER, *Phil. Mag. A* **75** (1997) 1171.
29. B. R. LAWN and M. V. SWAIN, *J. Mater. Sci.* **10** (1975) 113.
30. B. R. LAWN, M. V. SWAIN and K. PHILIPS, *ibid.* **10** (1975) L1236
31. B. WOLF and P. PAUFLER, *Surf. Interface Anal.* **27** (1999) 592.
32. J. STADLER, R. MIKULLA and H.-R. TREBIN, *Verhandl. DPG (VI)* **32** (1997) 830 M6.1.
33. PH. EBERT, M. FEUERBACHER, N. TAMURA, M. WOLLGARTEN and K. URBAN, *Phys. Rev. Lett.* **77** (1996) 3827; *Verhandl. DPG (VI)* **32** (1997) 830 M6.2.

Received 25 November 1997
and accepted 8 June 1999